Xinxiang Zhu*, Craig L. Glennie, and Benjamin A. Brooks

Automated near-field deformation detection from mobile laser scanning for the 2014 M_w 6.0 South Napa earthquake

https://doi.org/10.1515/jag-2021-0023
Received April 7, 2021; accepted November 4, 2021

Abstract: Quantifying off-fault deformation in the near field remains a challenge for earthquake monitoring using geodetic observations. We propose an automated change detection strategy using geometric primitives generated using a deep neural network, random sample consensus and least squares adjustment. Using mobile laser scanning point clouds of vineyards acquired after the magnitude 6.0 2014 South Napa earthquake, our results reveal centimeter-level horizontal ground deformation over three kilometers along a segment of the West Napa Fault. A fault trace is detected from rows of vineyards modeled as planar primitives from the accumulated coseismic response, and the postseismic surface displacement field is revealed by tracking displacements of vineyard posts modeled as cylindrical primitives. Interpreted from the detected changes, we summarized distributions of deformation versus off-fault distances and found evidence of off-fault deformation. The proposed framework using geometric primitives is shown to be accurate and practical for detection of near-field off-fault deformation.

Keywords: Near-field change detection, Mobile Laser Scanning (MLS), point cloud segmentation, deep neural network

1 Introduction

High-resolution mapping of surface deformation caused by earthquakes is important for both earthquake hazard mitigation and increased understanding of earthquake fault dynamics [1]. Various geodetic observations and strategies for estimating change have been developed to capture earthquake ground deformation. However, few current techniques have the ability to deliver accurate (cm-level) and high resolution (decimeter level spacing) fields of distributed displacements for an earthquake in the near field (i. e. closer than 200 m to the fault trace). Global navigation satellite system (GNSS) data is able to estimate static [2] and dynamic [3, 4] seismic displacement with subcentimeter precision. However, the spatial coverage of GNSS data is restricted by the spatial distribution of the GNSS receivers which are generally too sparse to monitor near-field fault deformation. Interferometric synthetic-aperture radar (InSAR) is also capable of delineating far-field earthquake deformation over a broad area with centimeter-level precision [5]. However, interferograms tend to decorrelate with spatial change and are vulnerable to large displacements and complex textures (such as vegetation) on the ground. Earthquake ruptures are characterized by complex deformation patterns, and a dislocated ground surface makes InSAR phase unwrapping near the surface deformation difficult [6, 7]. Optical imagery datasets can also be used for deformation detection [8], but only provide horizontal motion, and in general are unable to provide better than decimeter level accuracy, even with high-resolution images [9]. Therefore, although all these geodetic observations serve as important products for post-earthquake analysis [10], none of them are currently capable of capturing high accuracy and high-resolution rupture deformation in the near field.

Two of the most commonly used strategies for near field earthquake deformation detection are correlation-based and registration-based change detection using either optical imagery or lidar. For example, Milliner et al. (2015) used an image correlation-based method to quantify the horizontal displacement of the 1992 M_w 7.3 Landers, California earthquake [11]. The method produced decimeter accuracy horizontally but does not provide vertical motion. The resolution of the correlation-based algorithm is also affected by the required size of the correlation search window. Larger window sizes are required for improved correlation but makes the technique insensitive to subtle local changes. Smaller window sizes will be more sensitive to subtle changes but in general lead to

***Corresponding author: Xinxiang Zhu,** Department of Civil and Environmental Engineering, National Center for Airborne Laser Mapping, University of Houston, Houston, TX, 77204, USA, e-mail: xzhu123@uh.edu, ORCID: https://orcid.org/0000-0003-3126-8299
Craig L. Glennie, Department of Civil and Environmental Engineering, National Center for Airborne Laser Mapping, University of Houston, Houston, TX, 77204, USA, e-mail: clglennie@uh.edu, ORCID: https://orcid.org/0000-0003-1570-0889
Benjamin A. Brooks, Earthquake Science Center, U.S. Geological Survey, P.O. Box 158, Moffett Field, CA, 94035, USA, e-mail: bbrooks@usgs.gov

noisier correlation results. 3D-based earthquake deformation using the iterative closest point algorithm (ICP) has been implemented using both lidar and structure from motion (SfM) point clouds, [12, 13, 14, 15], for example. Zhang et al. (2015) used ICP to estimate earthquake deformation for the 2010 M_w 7.2 EI Mayor-Cucapah earthquake [14], Scott et al. (2018) estimated deformation for the M_w 7 2016 Kumamoto, Japan earthquake [13], and Scott et al. (2020) used ICP to estimate the long term creep rate for a section of the Central San Andreas and Calaveras faults [15]. The ICP method using airborne laser scanning (ALS) observations works well when expected displacements are larger than the decimeter-level uncertainty [9]. The spatial resolution of ICP is also limited by the size of the correlation window which is generally 20 to 100 meters [13, 14, 15, 16, 17, 18, 19]. ICP assumes uniform deformation within the correlation windows (e. g. [20]) and therefore the method may artificially smooth near-field deformation estimates. Both image-based correlation and ICP implicitly assume that spatial features within the search window are rigidly transformed and not deformed during the earthquake. The search window size has to be chosen wisely to balance detection resolution (using a smaller window size) and robustness (using a larger window size). It is challenging to keep this balance in the near field due to the complex geometry of the topography, the nonlinearity of the deformation pattern, and possible incomplete representation of the scene due to data occlusions.

Compared with ICP and image correlation, geometric model-based change detection removes the constraint of rigid deformation within a search window. Geometric model-based methods interpret the point clouds using models with simple geometry, i. e. geometric primitives. Changes are derived by tracking primitive movement between epochs. Kusari et al. (2015) showed that sub-centimeter level changes can be estimated by matching geometric models of building walls and roofs which are estimated from point clouds captured on planar surfaces [21]. Their method shows the potential for high-accuracy change detection using a sparse and redundant representation of the point clouds with simple geometric primitives. However, this method cannot estimate fault displacement from a single planar geometric primitive because it is only sensitive to motion along the plane normal; therefore several surfaces need to be amalgamated to estimate 3D displacement. In contrast, DeLong et al. (2015) used manually identified fence-posts and a cylindrical model to directly show centimeter-level changes from the 2014 M_w 6.0 South Napa earthquake [22]. The difference in pre- and post-event 3D cylinder locations was able to directly provide estimates of surface displacement for each post. Although these initial results were promising, the fence posts had to be manually identified and modeled. We propose an automated method of geometric primitive identification, matching, and displacement estimation to provide a more widely distributed model of earthquake deformation.

Using mobile laser scanning (MLS), we acquired 3D point clouds representing the geometry of fault-related surface displacements with sub-centimeter accuracy for the 2014 M_w 6.0 South Napa earthquake [23, 24]. Minimal coseismic offset, including coseismic and early postseismic displacements 7 days after the earthquake,[1] is detected by monitoring deformation of planar primitives representing the geometry of vineyard rows which were straight prior to the earthquake. Cylindrical primitives are generated with a workflow relying on PointNet [25], RANdom SAmple Consensus (RANSAC) [26], and least squares fitting. Postseismic surface displacements are detected by tracking the cylindrical primitives between epochs of MLS data collected 7 and 34 days after the earthquake, and it is shown that this method has the ability to detect centimeter-level ground displacement in the near field at sub-centimeter level precision. The detection results provide new observations of fault-related surface displacements with high-resolution and accuracy. Distributed ground displacements detected near the fault trace are important for the study of rupture mechanisms for active faults. The proposed semantic primitives can be implemented in automated point cloud-based change detection and automatic point cloud segmentation.

The rest of this paper is organized as follows: The MLS datasets from the 2014 M_w 6.0 South Napa earthquake are briefly described. The change detection strategy is demonstrated in the methodology section. Change detection results are presented for coseismic response, fault trace estimation, and postseismic deformation detection. Continuity of the rupture zone is interpreted and discussed followed by analyses of off-fault deformation distribution and uncertainties within the detection results.

2 MLS survey and dataset for the 2014 M_w 6.0 South Napa earthquake

The M_w 6.0 South Napa earthquake of 24 August 2014 was the largest earthquake in over 25 years for the San Fran-

1 For simplicity, we refer to the detected coseismic and early postseismic displacements 7 days after the earthquake as coseismic offset for the rest of the paper.

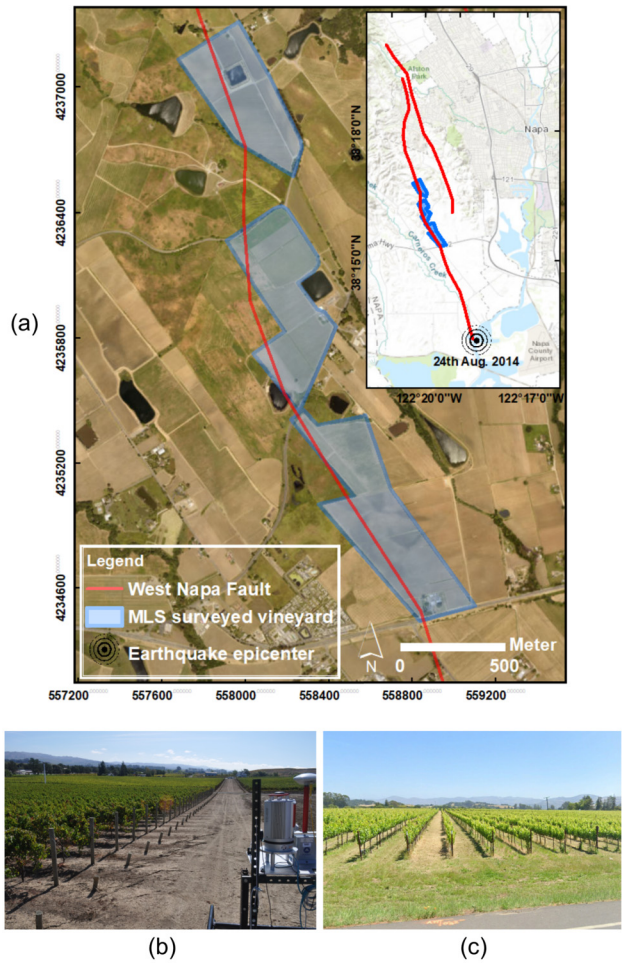

Figure 1: Overview of MLS survey area (a). Mobile laser scanner and images of vineyard rows (b, c).

cisco Bay Area, causing over half a billion dollars of economic damage. The earthquake was nucleated on the active West Napa Fault, a right-lateral strike-slip fault. In situ measurements were made documenting the coseismic surface displacements ranging from 5–50 cm largely confined to the Great Valley Group – bedrock resulting from Mesozoic forearc basin sedimentation – in the northern part of the rupture, whereas shallow afterslip occurred within a Quaternary alluvial basin to the south [27, 28]. Two MLS surveys [23] were conducted to document earthquake deformation using a RIEGL VZ-400 scanner; the first survey was on September 1 and 2, 2014 and the second on September 28–30, 2014. Laser point density was approximately 280 points per square meter at a distance of 50 m from the scanner.

Our study area is a subset of the MLS survey and comprises several vineyards where the fault trace crossed the vineyard rows approximately perpendicularly. Figure 1 shows the study area and representative pictures of vineyard rows. The average vine row length is approximately 250 m with anchor posts at two ends spanning each row. The average interval between rows is approximately 2.3 m. Vineyard rows were originally constructed to be straight lines with constant intervals between plants to maximize sunshine, therefore, any curvature, dislocation of tiles and posts can be confidently attributed to the 2014 South Napa earthquake [23]. Minimal coseismic offset is estimated in the first MLS survey; postseismic surface displacements are monitored between the two MLS surveys. Because of the primarily dextral nature of the Napa earthquake, we focus our method to examine only the horizontal components of deformation.

3 Change detection methodology

The key concept of the proposed change detection strategy is to represent MLS point clouds with geometric primitives and derive changes by tracking these primitives between temporally spaced datasets. Geometric primitive is a term from computer vision referring to simple geometry of an object that can be described by an equation with a number of free parameters [29]. In this case, geometric data are unordered lists of MLS point returns in three-dimensional Cartesian space and simple geometries are planar and cylindrical primitives representing outlines of objects scanned by the lidar scanner. With augmentation by additional semantics, planar vineyard row primitives and cylindrical fence post primitives are generated from MLS point clouds. As sparse and redundant representations of point clouds, geometric primitives are highly effective geodetic markers that can be temporally tracked to reveal ground displacement.

The total near-field displacement consists of on-fault brittle deformation in the principal and secondary fault zone, and off-fault deformation [30, 11]. Figure 2 is a schematic drawing of planar features crossing the synthetic surface ruptures of an earthquake, and the objectives of the proposed change detection are to:

- Delineate fault trace locations.
- Quantify near-field displacements within approximately 200 m of the fault trace.
- Summarize displacement distributions versus off-fault distance.

Table 1 shows the basic change detection strategies with detailed descriptions of the methodology given in the following sub-sections.

3.1 Change detection using planar primitives for coseismic response

Coseismic response is approximated using offsets from planar primitives modeled from the top part of the scanned vine row. Each vine row is cropped using a bounding box with a width of 3 m and defined by the posts located at the ends of each row, where post locations are manually digitized from the MLS data. The top 20 cm portion of each row is automatically extracted and analyzed using a moving window. Due to scanner occlusions for the lower part of the vines, only the top part of the vine point clouds are extracted to ensure complete spatial coverage. A 2D plane is constructed spanning the post locations with the planar normal parallel to the ground. Deviations from this plane estimate vine row dislocation due to the Napa earthquake, and normal distances from this plane are calculated which approximate total coseismic offsets.

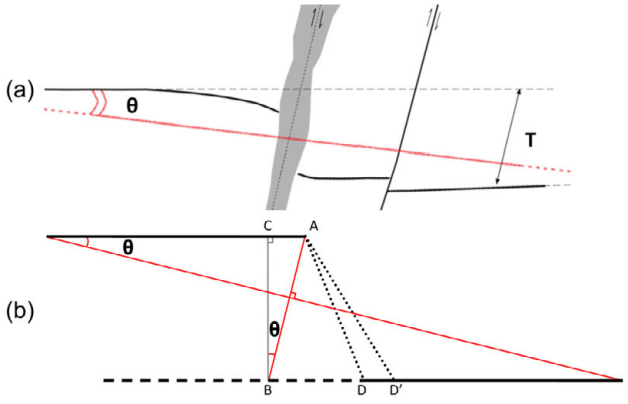

Figure 2: Schematic (a) and geometric (b) drawing of planar features crossing the surface rupture (grey zone). Total near-field displacement is labeled as T. Given that the row length (about 250 m) is about 500 time larger than the displacement (about 50 cm) the angle θ is small enough ($1 - \cos\theta \approx 2 \times 10^{-6}$) that the deviation from the reconstructed plane (**AB**) serves as a good approximation of the minimum coseismic offset (**BC**). Note that the offset does not reflect the true estimates of accumulated deformation (**AD** or **AD'**) as surface rupture was expressed as en echelon fractures. Figure (a) adapted from a graphic given in [30].

With raw MLS data as input, point clouds within the moving window are filtered to remove outliers based on distances to nearest neighbors [31], and offsets from planar primitives are calculated as averaged point-to-plane normal distances within a 1 m window. Turning points are detected where the offsets change signs. A series of consistent turning points are used for an estimation of a digital fault trace. Given that the row length (about 250 m) is about 500 times larger than the displacement amount (about 50 cm), the angle (θ in Figure 2) between the plane normal and dislocation direction is small enough ($1 - \cos\theta \approx 2 \times 10^{-6}$) that deviation from the reconstructed plane (detected as minimal coseismic offset) serves as a good approximation of the coseismic response. Repeating this process over all the extracted rows, distributed horizontal displacements are derived estimating the minimum coseismic offset along the fault trace. Note that we cannot guarantee that both (a) the vine rows were completely straight before the earthquake and (b) the posts' locations selected as end points accurately depict the optimal plane location. Therefore, the offsets from the planar primitive should not be evaluated as true estimates of accumulated deformation (Figure 2(b) **AD**) but rather the minimum coseismic offset (Figure 2(b) **BC**) approximated by the planar residuals as (Figure 2(b) **AB**). However, these deviations from the plane do enable an accurate estimation of the fault line location and also allow the examination of displacement curvature near the fault.

3.2 Change detection using cylindrical primitives for postseismic surface displacement estimation

Postseismic surface displacement is estimated using the displacement of cylindrical primitives between two temporally spaced MLS surveys. To model the cylindrical primitives, which represent scanned posts at the end of each vine row (Figure 4), the point clouds first need to be segmented. In previous work, the segmentation was manually

Table 1: MLS change detection strategies.

Process	Change detection for minimal coseismic offsets	Change detection for postseismic surface displacements
Input data	Point clouds of the top of vine rows	Point clouds representing vineyard posts
Primitive type	Planar primitives defined by vinerow end posts	Cylindrical primitives extracted using PointNet [25], filtered using RANSAC and modeled using a least squares adjustment
Detection methods	Measure point to plane distances	Cylindrical primitive locations observed at two epochs
Output instances	Total deformation of 1300 vine rows 7 days post earthquake, and estimation of the fault trace	Displacements of 2600 posts between 7 and 34 days post earthquake

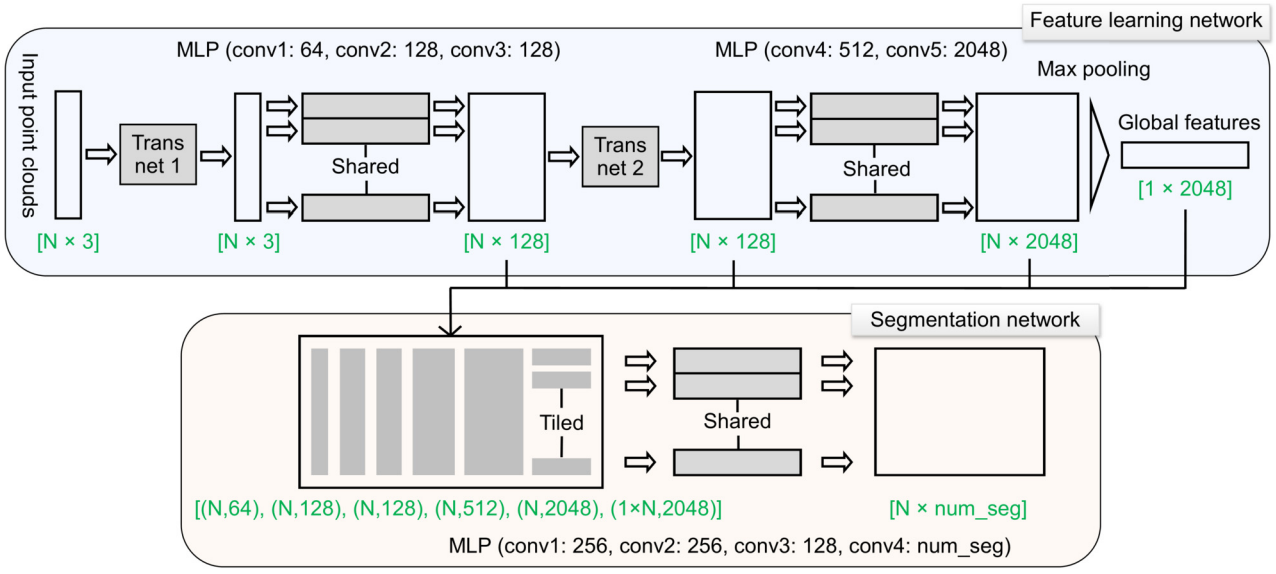

Figure 3: Schematic Structure of PointNet [25]. Feature learning network on top, and segmentation network on bottom.

performed [22]. To automate this process, we implement a deep neural network – PointNet [25] to automatically segment the MLS point clouds. The segmented datasets are later filtered using RANSAC [26] and modeled as primitives using a least squares adjustment. Displacements are derived by tracking the relative motion of the cylindrical primitives between the two epochs of MLS data.

3.2.1 PointNet: Automated point cloud segmentation

PointNet, proposed by [25] is a unique deep neural network that directly works on 3D point clouds. The method and its variants have been applied as a common strategy for lidar point cloud semantic segmentation (e. g. [32, 33, 34, 35]). The network learns a set of optimization functions selecting informative points and aggregates the optimization results as global descriptors. Fully connected layers and symmetric max-pooling functions are implemented to handle the irregular format of point clouds. Figure 3 shows the basic structure of PointNet for point cloud segmentation. The network consists of two major parts: a feature learning network that learns with fully connected layer structures ended with a max-pooling layer and a segmentation network that augments learned local and global features and outputs per point labels as segmentation results.

For supervised learning on point clouds, we set up a vine row training set where 120 scanned vineyard row point clouds are manually labeled, consisting of 9 million total labeled points. Every point within this set falls

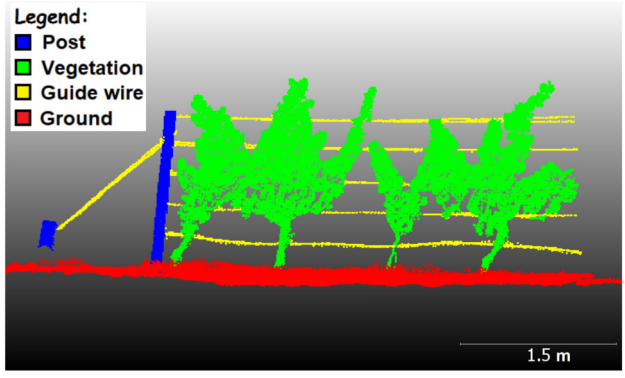

Figure 4: Segmentation example for a portion of a single vine row. MLS point clouds were automatically segmented into four categories using PointNet.

into one of four categories – (1) posts, (2) vegetation, (3) guide wire and (4) ground. Random sampling from this training set generates over 40 thousand training samples, where each sample consists of 2048 points in a single vine row. The train-validation-test split is 7:1:2. Figure 4 shows a segmentation example where point clouds were automatically segmented into the four categories. After training, the network is capable of processing all 2600 scanned sections of vineyard posts, which consist of over 300 million MLS laser returns. The point clouds were automatically segmented into the four categories and the posts were then extracted for cylindrical primitives modeling. Herein, only the end posts are analyzed because the middle posts were often occluded by the vine row vegetation.

3.2.2 Cylindrical primitives modeling

The segmented posts were modeled as cylindrical primitives and then pre- and post-deformation primitives were clustered by their locations. A Gauss-Helmert model [36] is used for least squares fitting of the cylindrical primitives:

$$g(l+e,p) = X^2 + Y^2 - r^2 = 0, \tag{1}$$

$$\text{where } \begin{bmatrix} X \\ Y \\ Z \end{bmatrix} = R_2(\phi)R_1(\omega) \begin{bmatrix} x_{obs.} \\ y_{obs.} \\ z_{obs.} - \overline{z_{obs.}} \end{bmatrix}, \tag{2}$$

$$R_1(\omega) = \begin{bmatrix} 1 & 0 & 0 \\ 0 & \cos\omega & \sin\omega \\ 0 & -\sin\omega & \cos\omega \end{bmatrix}, \tag{3}$$

$$R_2(\phi) = \begin{bmatrix} \cos\phi & 0 & -\sin\phi \\ 0 & 1 & 0 \\ \sin\phi & 0 & \cos\phi \end{bmatrix}, \tag{4}$$

where the inputs are MLS laser returns for a single post $[x_{obs.}, y_{obs.}, z_{obs.}]^T$ with measurement uncertainties e. The point clouds are shifted and rotated so that a cylinder can be estimated at the center of each cloud with a vertical axis. The estimated parameters p are shift components (X, Y), and rotation angles (ω, ϕ) for the x- and y-axis. The radius r of the cylinder is fixed at 5 inches (12.7 cm) for the observed anchor posts.

The top face of a scanned post is usually missing or occluded by vegetation due to the sideways field of view of the mobile scanner. As a consequence, the height of each cylinder (shift component Z) is left as a free parameter and the horizontal location of the model is estimated at the mean height of every point cloud to reduce shift-rotation correlations. Because of uncertainties in the lidar measurements and mis-segmented points from PointNet, we embed a RANSAC algorithm to improve the robustness of the least squares fitting. The RANSAC function is initialized with mean and principal directions of the point clouds for shift and rotational components. Final modeling results are estimated through a least squares adjustment using the optimum RANSAC parameters and estimated inlier points. Figure 5 shows an example of the adjustment results.

Results from RANSAC and the least squares adjustments are cylindrical primitives of the fence posts with geometry characterized by the posts central locations and orientations. Propagation along the cylinder axis gives intersections of the posts with the ground. Using ground points segmented from PointNet, intersections are extracted. Corresponding intersections before and after the deformation are clustered and differenced to estimate ground displacement between the two MLS surveys.

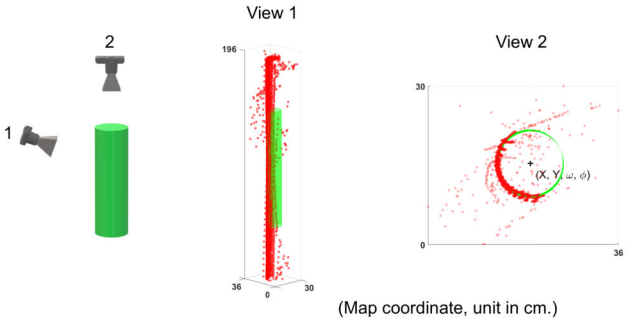

Figure 5: Example of a cylinder primitive. Red dots are segmented MLS points, and the green cylinder shows the optimal fit modeled primitive.

4 Detection of earthquake-related surface displacements

Using the planar and cylindrical primitives, the surface displacement field of the fault is determined. Minimal coseismic offset is estimated by quantifying the vine row deformation from the first MLS survey by calculating deviations from a planar primitive. Postseismic deformation is estimated by tracking cylindrical primitives and their ground intersections between the two MLS surveys.

4.1 Coseismic response detection

Figure 6 displays minimal coseismic offset detected using planar primitives. Dextral displacement magnitude is color-coded as the deviation from each planar primitive. Right-lateral motion of the fault is characterized by the consistent red to blue color change across the fault. The fault trace is estimated by mapping the transition from red to blue for every planar primitive where a consistent strike, expanding north-south, can be modeled by connecting adjacent transitions throughout the surveyed area. This fault trace approximates the surface projection of the fault. Given the intersections where the fault trace traverses planar primitives, a digital fault trace (black line in Figure 6) is estimated using robust local linear regression (LOWESS) [40]. This fault trace is piecewise linear due to the regression model. Employing this derived digital fault trace, statistics for off-fault directions can be calculated.

Modeling the digital fault trace serves as a good supplement for field reconnaissance of the fault ground rupture given that (a) on site surveys of ground ruptures can be localized and inconsistent over kilometer scales. An earthquake and its induced geo-hazards may limit the access to zones of deformation along the surface faulting,

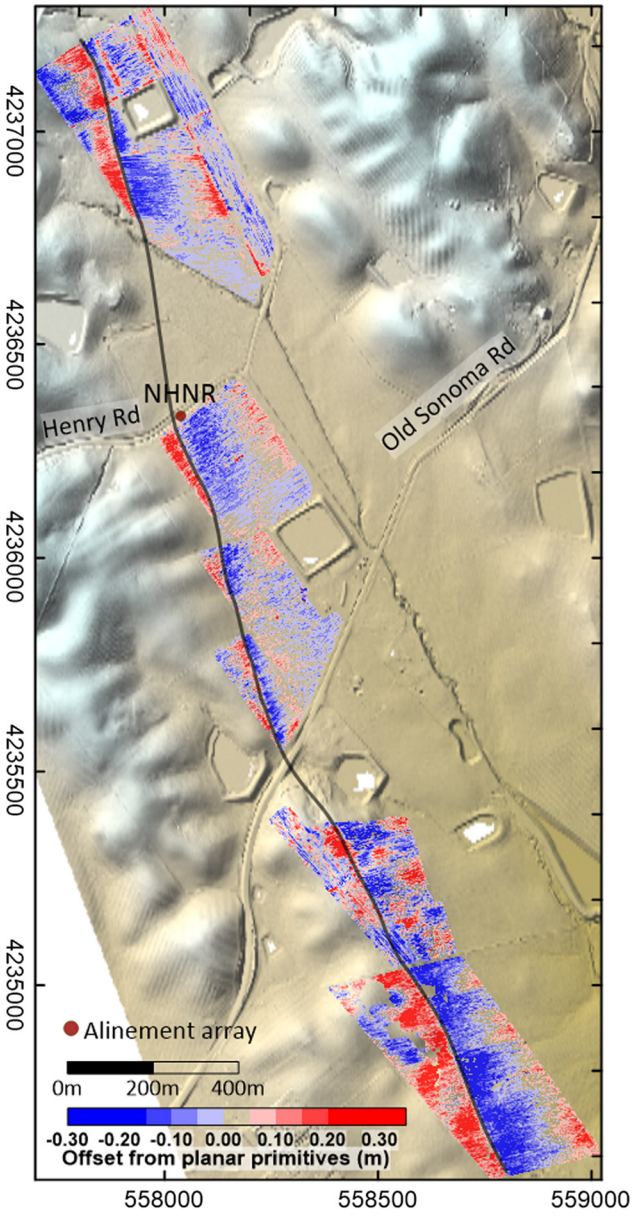

Figure 6: Minimal coseismic offsets approximated by the deviations from planar primitives. Offsets are color-coded and the estimated fault trace is given as the black line. Relief base map is generated from airborne laser scanning (ALS) data [3]. Field measurements of coseismic displacements are available at the fault crossing of Henry Road [37, 38]; alignment array measurements of postseismic surface displacements are available at station NHNR [39].

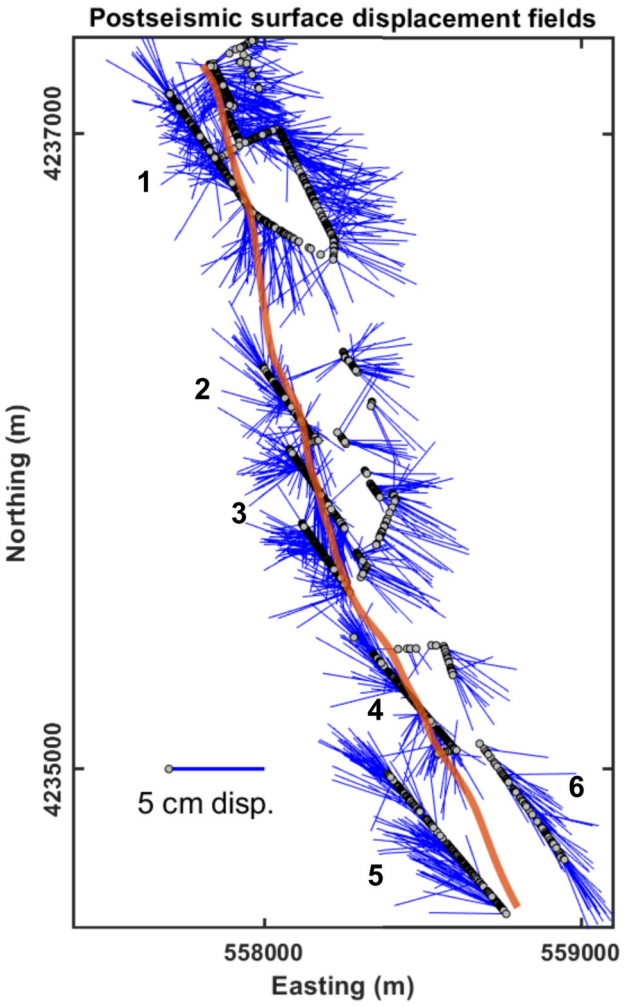

Figure 7: Postseismic surface displacement fields detected using cylindrical primitives. Orange solid line shows the fault trace. Surveyed area is subdivided with numbers indicating areas of study for upcoming analyses. The pin arrowhead depicts the location of detection where the length and orientation of each arrow represents the amount and direction of postseismic surface displacement.

and important displacement signatures could be missed by a field survey if the displacement is not associated with significant cultural feature damage [38, 41, 42]. (b) the slip front of the fault can be buried without reaching the surface and expressed by insignificant ground displacement or scattered ground cracks instead of obvious ground ruptures [23, 24]. This method estimates the fault trace from redundant primitive measurements throughout the area; therefore, the estimated fault trace is less vulnerable to local anomalies and more consistent spatially. The automated process also has the potential for delivering a ground rupture map in a timely manner post earthquake.

4.2 Postseismic surface displacement detection

Figure 7 shows the horizontal displacement of cylindrical primitives in between the two MLS surveys. Each line on the map represents the path of displacement for a single post tracked at its ground intersection. Tracking more than

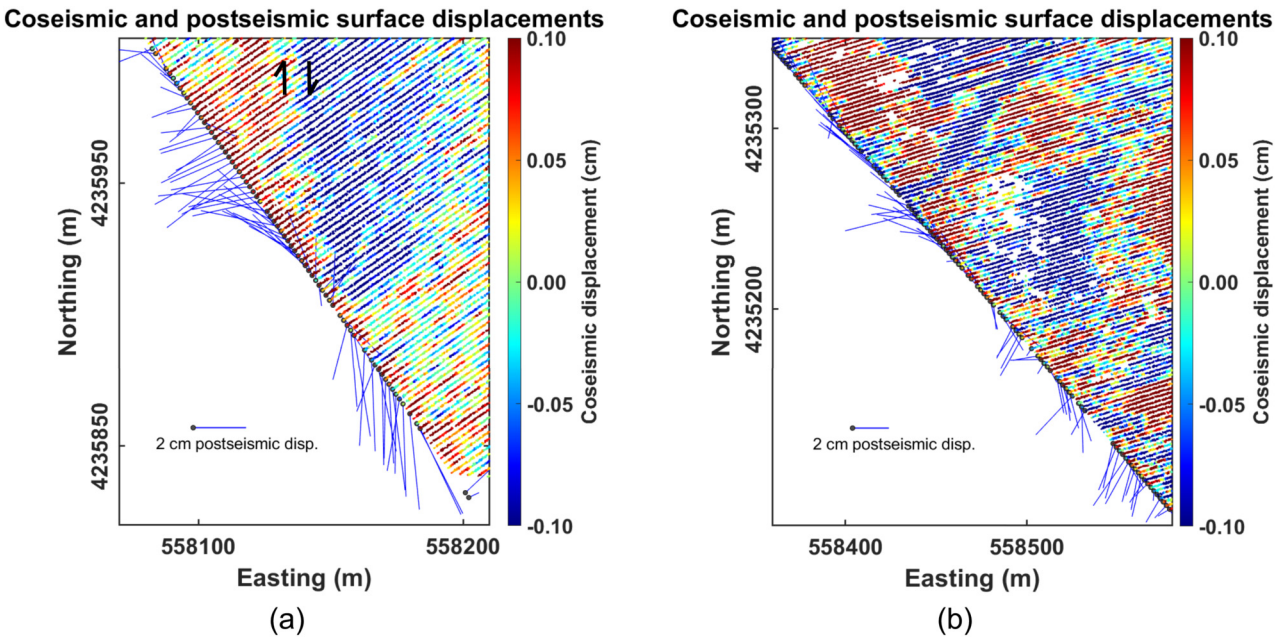

Figure 8: Overlap of planar residuals and postseismic change detection results (a, b) for study areas 3 and 4 in Figure 7. Planar residuals are color-coded by magnitude of minimal coseismic offsets; the symbol of strike-slip indicates the location of the fault trace. The pin arrows depict the postseismic displacements detected using cylindrical primitives where the length and orientation of each arrow represents the amount and direction of postseismic surface displacement. (a) The red-blue margin delineates the coseismic fault trace; the distributed arrows localize the postseismic fault crossing. Inflection points from the detected minimal coseismic offset are collocated with the change in arrow directions where adjacent arrows change direction dramatically. This confirms the consistency of the change detection results as the transition in both coseismic and postseismic displacements are colocated.

2600 cylindrical primitives' displacements, postseismic surface displacement fields in the near field are revealed. The detected displacement field quantifies the surface displacement between Sep 1st and Sep 30th, 2014 which are 7 and 34 days after the mainshock. Local shear patterns are found where the fault trace crosses between successive posts (Figure 8, Figure 9(a–d)). Colocated with the planar residual approximation to coseismic response, Figure 8 shows the consistency of the detection results using two kinds of geometric primitives. Planar primitives tracking coseismic response and cylindrical primitives estimating postseismic surface displacements are colocated at the fault trace, which validates the location of the ground rupture. While the planar primitives can only provide 1D displacement as deviations from straight vine rows, the cylindrical primitives provide 2D displacement vectors showing local deformation in the near field.

Subtle postseismic surface displacement fields are revealed from changes detected using cylindrical primitives. Figure 9 shows six local displacement patterns. Subplots a–d show local shear patterns where the fault trace crosses a line of successive posts. The lines represent vine row post displacements from Sep 1st to Sep 30th. To track how linear features on the ground are deformed by the fault, adjacent posts are connected by local regression lines. Each node of the line represents a post's location at that epoch and the curvature of the line represents nonlinear local deformation induced by shear. Local shear patterns are found in those cases characterized by the transition of surface displacement directions and entangled pre- and post-deformation regression lines. Spinning patterns are found where the fault trace traverses lines of posts.

Constant strike-slip displacements are observed at posts located on either side of the fault, shown in cases 5 and 6 in Figure 9(e) and (f). The displacements show little variation in direction and scale. The isotropic displacement patterns for cases 5 and 6 indicate little or no off-fault deformation at these locations.

5 Interpretations and discussion

Compared with previous geodetic change detection results, the proposed strategy successfully reveals the 2D near field horizontal deformation for the 2014 South Napa earthquake. Though focused on sensing horizontal com-

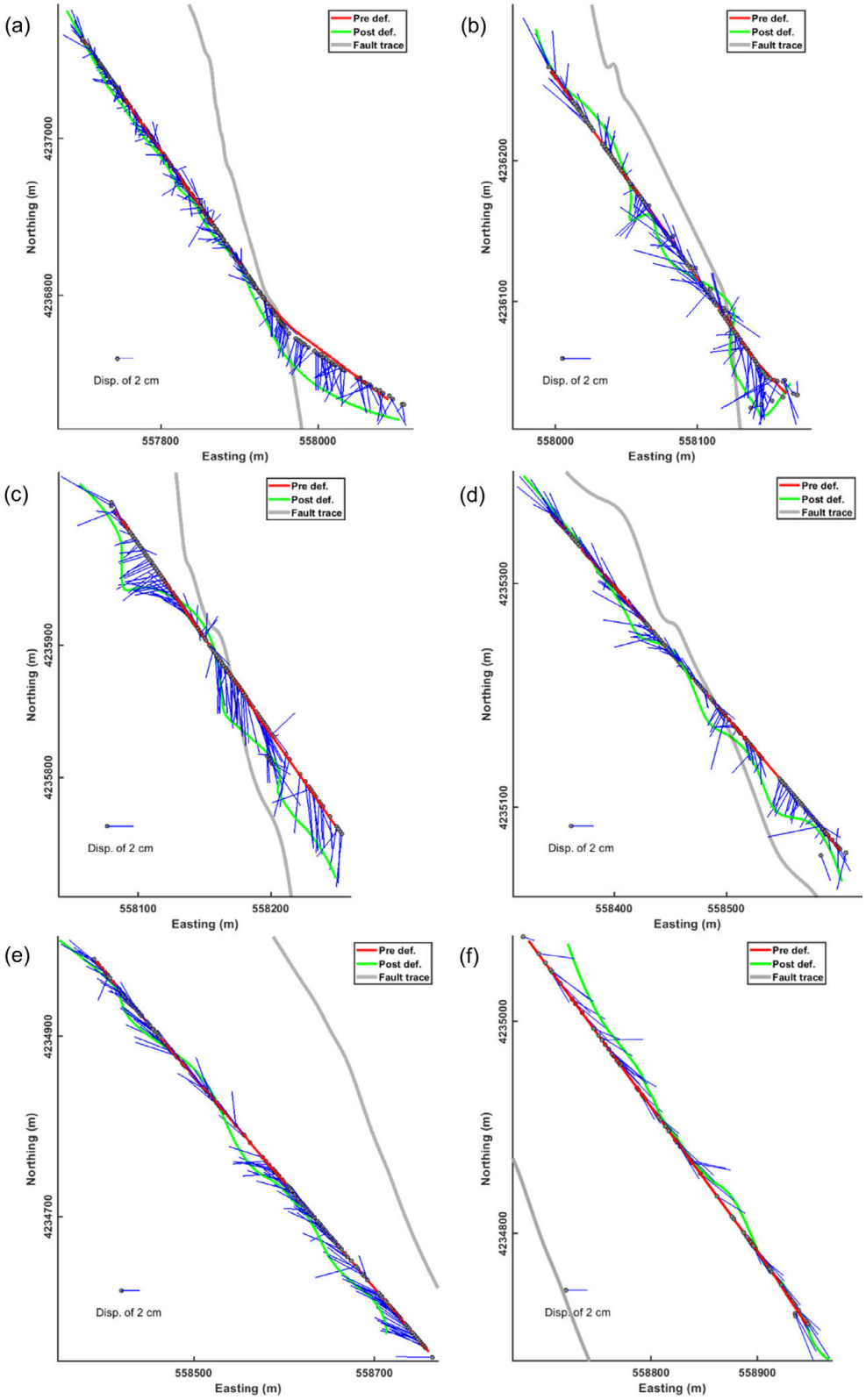

Figure 9: Postseismic surface displacement patterns for the six study areas numbered in Figure 7 (case 1–6 as a–f). The pin arrows show the detected postseismic surface displacements; the arrow head depicts the location of the detection where the length and orientation of each arrow represents the amount and direction of postseismic surface displacement. Regression lines show how linear features are deformed at the fault crossing due to postseismic deformation. Red and green lines represent vineyard post locations captured by MLS surveys 7 and 35 days after the Napa earthquake.

ponents, cylindrical primitive-based change detection can also reveal 3D deformation where vertical components are derived by differencing the intersections of the primitives with the ground. However, the estimated vertical component does not benefit from the redundancy of the cylindrical model, and thus the uncertainty of the vertical component directly depends upon the vertical point cloud accuracy. It is challenging to model the top and bottom face of a cylindrical post given poor data coverage from the sideways field of view of a mobile platform. Considering the dextral displacement pattern, we only provided horizontal components of our change detection results.

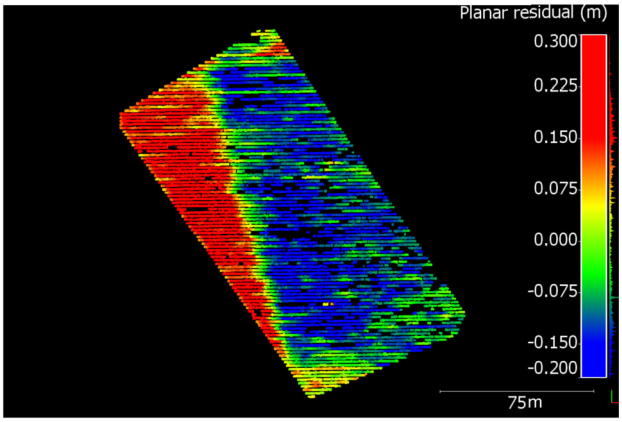

Figure 10: Zoomed-in plot of planar residuals which approximate minimal coseismic offset at the fault trace. Color changes smoothly over the fault trace.

5.1 Continuity analysis of the rupture zone

Continuous vine row curvature over the region indicates that the principle rupture remains buried under the ground, whereas a constant dislocation discontinuity at the surface would indicate that either the fault front reached the ground surface or a secondary fault zone exists. Figure 10 shows a zoomed-in map of the planar expression of coseismic response with color-coded planar residual magnitude. The color at the fault trace changes smoothly, indicating no discrete fault patches exist. Such a continuous displacement pattern is found throughout the surveyed area and is consistent with the analyses that the fault rupture remained buried. The smooth intersection reflects the characteristics of a fault trace where surface displacements are comprised of en echelon sheared extensional fractures and linear 'mole tracks'. This pattern is consistent with in situ measurements from [27], and [28], and shallow fault slip modeling presented in [23] and [24].

5.2 Distributions of deformation versus off-fault distance

Postseismic surface displacement distribution versus off-fault distance provides evidence highlighting non-brittle deformation within the detected changes. The metric for off-fault distance is calculated as the perpendicular distance from observation locations to the closest linear fault

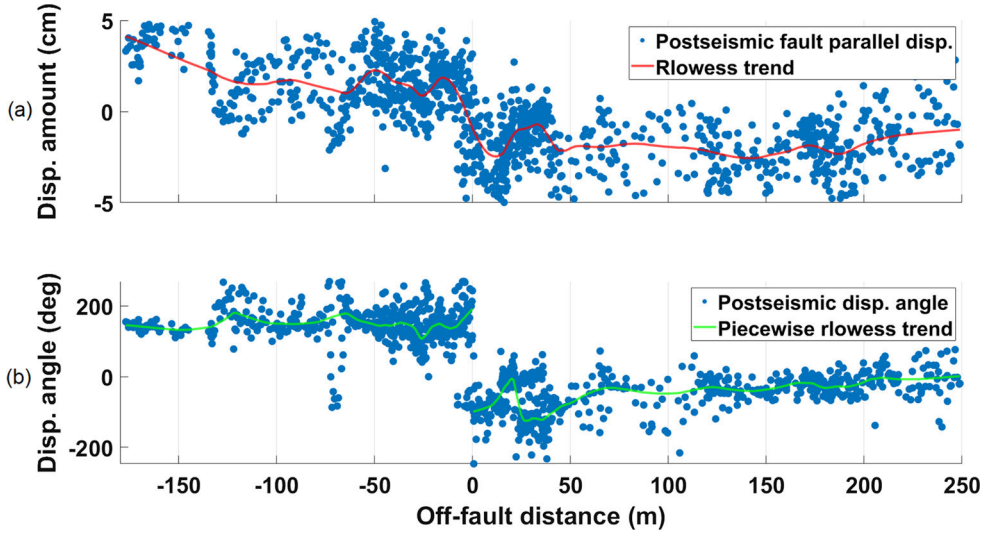

Figure 11: Off-fault distributions of postseismic surface displacements. Components of postseismic fault parallel displacements (a) and displacement directions (b) are plotted versus off-fault distance. Fault parallel component is determined from the strike of the nearest fault section. Robust local linear regression trends are provided to highlight the off-fault distribution pattern.

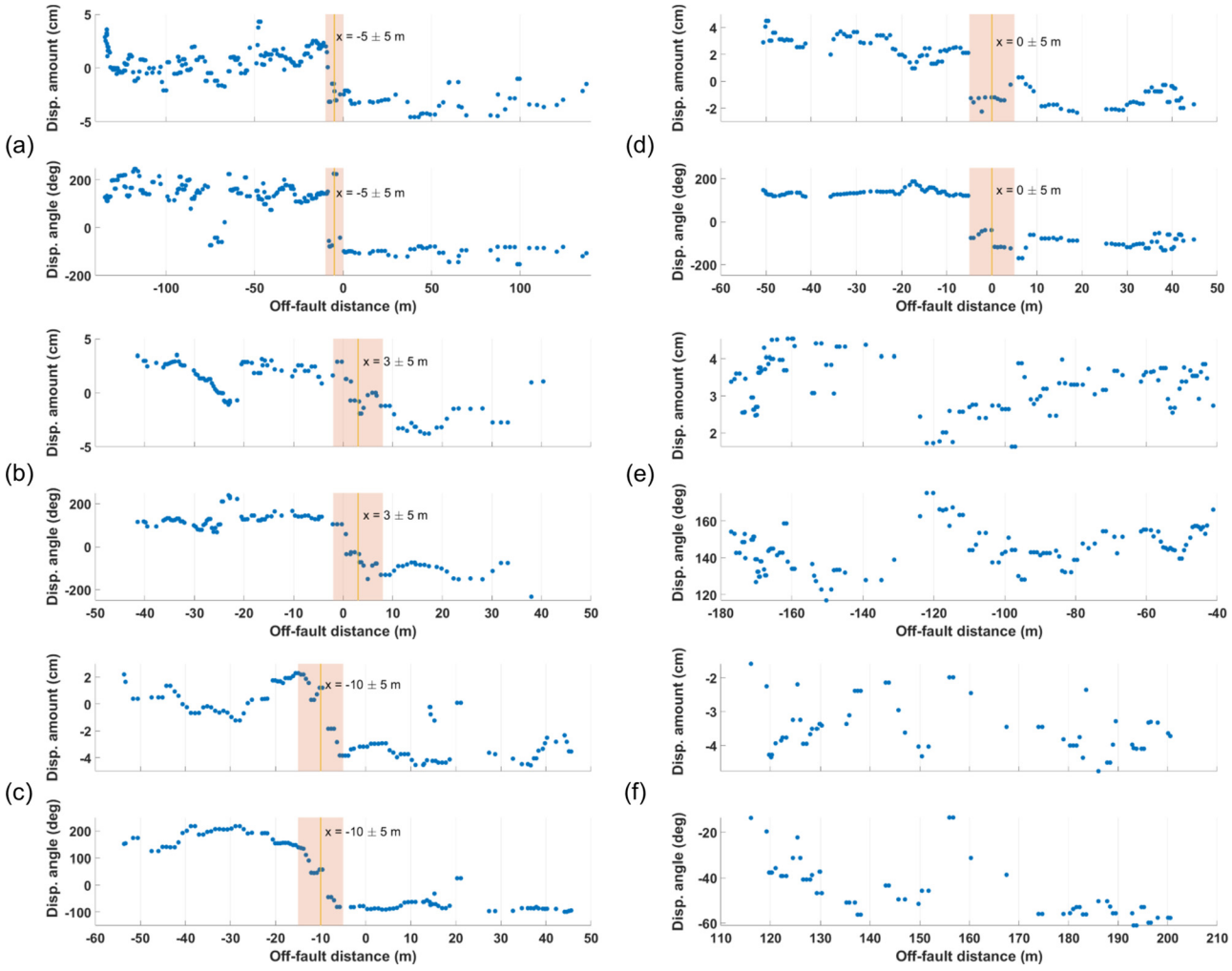

Figure 12: Off-fault distributions of postseismic displacements for the six study areas in Figure 7 (case 1–6 as a–f). For each case, two distributions are provided: distribution of fault parallel displacements (top) and displacement angle (bottom) plotted versus off-fault distances. The fault parallel component is determined from the strike of the nearest fault section. An ≈10 m transition zone is estimated visually at the fault crossing for areas 1–4.

trace segment estimated using the planar primitives. Because the posts are anchored at various distances from the fault trace, off-fault distances are spread out uniformly across the rupture zone. Postseismic surface displacements are projected along the fault trace direction as fault parallel displacements. Off-fault deformation is expressed as the profile of fault parallel displacements.

Figure 11 shows the results where fault parallel displacements and postseismic displacement directions are distributed over a range of off-fault distances. Nonparametric robust local linear regression trends was used to highlight the displacement distribution pattern without introducing assumptions for local fault mechanics. The dextral pattern is obvious in the displacement angle plot where two dominant sliding directions are identified as −51.33° and 145.51° from the East. Angular variances are larger close to the estimated fault trace and smaller further away. The dextral pattern is also confirmed by the displacement magnitude transition at the fault trace.

Figure 12 shows the same off-fault displacement plots for the six study areas corresponding to Figure 7. Areas 1–4 (Figure 12 a–d) show about 3 cm of off-fault deformation within approximately 10 m of the fault trace. This 10 m transition zone is estimated visually and highlighted in the figure for the area 1–4 fault crossings. The corresponding angular profiles show transition of displacement angles as a result of crossing the fault. Cases 5 and 6 (Figure 12(e, f)) show no sign of off-fault deformation as these profiles do not cross the fault trace and show little variation in displacement magnitude and angle compared with cases 1–4.

Table 2: Average postseismic fault parallel displacements for the six study areas in Figure 9, in centimeters (standard deviation in brackets). Displacements for each side of fault do not include 10 m transition zone.

Study area	West of fault	East of fault	Difference
1	0.79 (1.27)	−3.09 (1.00)	3.88 (1.62)
2	1.71 (1.27)	−2.32 (1.34)	4.03 (1.84)
3	0.51 (1.06)	−3.29 (1.22)	3.79 (1.61)
4	2.65 (0.83)	−1.28 (0.74)	3.93 (1.11)
5	– (–)	– (–)	3.29 (0.70)
6	– (–)	– (–)	−3.47 (0.76)

Table 2 shows the corresponding postseismic fault parallel displacement for each side of the fault outside the transition zone.

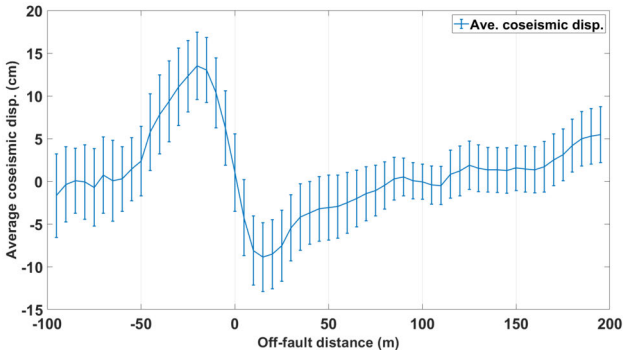

Figure 13: Planar residual estimate of minimal coseismic offset averaged over 1300 vine rows. Error bar indicates local displacement variation within 10 meter bins of off-fault distance.

5.3 Potential errors within the change detection results

Because both coseismic and postseismic surface displacements are calculated as relative changes, the majority of residual systematic errors for the MLS and any geodetic datum biases will not affect the calculated relative deformation. Given that coseismic and postseismic surface displacements are resolved from unique data collections after the earthquake, there are no repeat observations of the same event for estimating uncertainty. However, the accuracy of the detection results can be evaluated by (a) comparing coseismic and postseismic surface displacements with field observed coseismic ground displacements and measurements of postseismic surface displacements at alignment array stations, and (b) by checking the internal consistency of displacements in areas that are believed to share similar deformation patterns. For example, spatially close vineyard rows crossing the fault at a similar angle should show coherent coseismic displacements distributed off fault; areas far away from the fault trace should show regional dextral postseismic displacements that are uniform for either side of the fault.

5.3.1 Validation with field observations and alignment array measurements

We can validate the accuracy of the detection results with field and alignment array observations collected near the fault crossing at Henry Road (Figure 6). Brocher et al. (2015) [37] recorded 40 cm right-lateral offset, rounded to the nearest centimeter, in the field north of Henry Road within two days after the earthquake. The field rupture was observed as a zone of en echelon left-stepping fractures, and approximate uncertainties for measured offsets are around 5 cm. Ponti et al. (2019) [38] recorded 40.9–46 cm strike-slip displacements at the same location using an estimated fault azimuth. They also point out that most of the surface rupture was expressed as disconnected left-stepping en echelon fractures several meters or more in length with measurable dextral displacements. Hudnut et al. (2014) [3], using alignment array postseismic displacement measurements and AFTER models inferred a 14 cm coseismic displacement at alignment array station NHNR. Our estimate of the minimal coseismic offset from the planar primitives is about 25 cm shown in Figure 13 which agrees with field measurements at the decimeter level. Our estimation is smaller than [37, 38] because (a) the detected minimal offset could underestimate the true accumulated displacement as explained in Section 3.1 (Figure 2), (b) estimating fault azimuth in the field might lead to an overestimate of the surface displacement, and (c) we are comparing localized in situ measurements near the fault crossing at Henry Road with a regional average estimated from all vine rows; the field measurement captures the most obvious displacements that can be accessed by an observer, but they are sparse and discontinuous and do not span the MLS survey area. The average may lead to smaller estimates of displacements from the MLS survey compared with localized field measurements which highlight expressions of displacement at single points.

After the earthquake, alignment arrays were installed to monitor the afterslip [39]. We validated our estimated postseismic surface displacement by comparing the to alignment array station NHNR located on Henry Road (Figure 6). Observed accumulated displacement at NHNR was 18.7±0.22 mm on September 1; 57.1±0.26 mm on September

19 and 76.1 mm on October 23 (error not available). Alignment array station NHNR is bounded by study areas 1 and 2 shown in Figure 7. Referring to Table 2, we estimated 3.88 ± 1.62 cm and 4.03 ± 1.84 cm postseismic surface accumulated displacement between September 1 and September 28. For the same time span, the estimated displacement at NHNR is 4.39 cm using alignment array observations and the AFTER program [43, 44, 45], which agrees at the level of 4–5 mm with our MLS estimate.

5.3.2 Change detection precision

The precision of the change detection results is determined by checking the internal consistency of the estimates. Minimal coseismic offset was estimated by modeling vine rows as planar primitives. The consistency of the planar deviations can be estimated by checking the coherence of the off-fault distributed deformation pattern. Given that the vine rows cross the fault trace at a similar angle, coseismic deformation from each vine row should show similar patterns distributed off fault forming a coherent deformation pattern across all vine rows. Figure 13 shows the minimal coseismic offset averaged over 1300 vine rows. The error bars represent the variation of the displacement magnitude within 10 meter windows. The overall scale of the error bar is relatively uniform and slightly decreases off the fault center which indicates a consistent pattern exists across all vine rows and complex deformation patterns exist near the fault trace. The error bars vary in size from 2 to 5 cm across the region. Note that variation of this pattern across different vine rows could also be due to partial occlusions in the lidar point clouds. The uneven vegetation growth along each vine row may bias the planar primitives and the occlusions of a lidar scan may result in incomplete planar primitives extracted from point clouds. Therefore, further field reconnaissance measurements would be helpful to determine probable sources of this variation and better quantify the accuracy of the coseismic offsets from MLS.

The uncertainties in the estimated postseismic surface displacements are evaluated by checking the consistency of observations located off the fault trace. Given the assumption that displacements further from the trace should be smoother and more locally coherent, the variation of the displacement detected in the far-field can serve as a good estimate of consistency. Referring to Figure 9(e and f) and Table 2, detected displacements for areas 5 and 6, with vine row posts on only one side of the fault, show a standard deviation of about 7 mm. Given that the methodology is consistent for all posts, we expect a similar level of precision (subcentimeter) for changes detected using cylinder primitives. The other cases (area 1–4) have larger displacement variation due to more complex deformation patterns captured near field, but still only show 10 to 15 mm of variation.

Coseismic and postseismic surface displacement detection results using planar and cylindrical primitives show internal consistency. Their off-fault displacement distribution also indicates a consistent ground deformation zone. Although the observed minimal coseismic offset has a larger magnitude in comparison with postseismic displacements observed between 7 and 34 days after the earthquake, they both show a maximum displacement approximately 25 m off the estimated fault trace (Figure 13 and Figure 11(a)). These coherent detection results confirm the consistency of the deformation estimates after the earthquake.

6 Conclusion and future work

In this paper, we developed a method of using automatically extracted geometric primitives to detect changes in the near field of an earthquake. Geometric primitives are shown to be an efficient representation of MLS point clouds for subtle change detection. A change detection workflow was developed relying on PointNet, RANSAC, and least squares cylinder fitting for geometric primitives modeling.

The methodology described successfully recovers the dextral deformation field of the 2014 M_w 6.0 South Napa earthquake. 25 cm coseismic offsets and 3–4 cm postseismic displacements are revealed with decimeter and centimeter level precision respectively over a study site three kilometers long. The fault trace is revealed using planar primitives, and local shear patterns are found from the postseismic displacement distribution detected using the cylindrical primitives. Dextral deformation distributions versus off-fault distances are summarized and off-fault deformation is detected. Results are validated comparing to field and alignment array observations, which show decimeter level agreement with field observations of coseismic offset, and sub-centimeter level agreement with postseismic displacement at an alignment array station.

The proposed primitive-based change detection strategy can be generalized as a framework for geological change detection. A project on aseismic fault creep detection using persistent urban geodeteic markers is in progress. For future work, we plan to augment our change

detection strategy using more generic geometric primitives and consider the addition of other high definition surveying observations into the methodological framework.

Acknowledgment: We thank Preston Hartzell for guidance in point cloud processing. We are grateful to Chelsea Scott and the other two anonymous reviewers whose constructive criticism helped to improve the manuscript.

Funding: Funding for this research was provided by a cooperative agreement from the USGS and two grants from the National Science Foundation (1347092 and 1830734).

References

[1] J. M. Stoker, J. C. Brock, C. E. Soulard, K. G. Ries, L. Sugarbaker, W. E. Newton, P. K. Haggerty, K. E. Lee, and J. A. Young, *USGS lidar science strategy: mapping the technology to the science*, US Department of the Interior, US Geological Survey, 2015.

[2] P. Segall and J. L. Davis, *GPS applications for geodynamics and earthquake studies*, Annual Review of Earth and Planetary Sciences, 25 (1997), pp. 301–336.

[3] K. W. Hudnut, T. M. Brocher, C. S. Prentice, J. Boatwright, B. A. Brooks, B. T. Aagaard, J. L. Blair, J. Fletcher, J. Erdem, C. Wicks, et al., *Key recovery factors for the August 24, 2014, South Napa earthquake*, US Department of the Interior, US Geological Survey, 2014.

[4] S. M. Alif, I. Meilano, E. Gunawan, and J. Efendi, *Evidence of postseismic deformation signal of the 2007 M8.5 Bengkulu earthquake and the 2012 M8.6 Indian Ocean earthquake in Southern Sumatra, Indonesia, based on GPS data*, Journal of Applied Geodesy, 10 (2016), pp. 103–108.

[5] M.-J. Jo, H.-S. Jung, and S.-H. Yun, *Retrieving precise three-dimensional deformation on the 2014 M6. 0 South Napa earthquake by joint inversion of multi-sensor SAR*, Scientific Reports, 7 (2017), pp. 1–10.

[6] R. Michel, J.-P. Avouac, and J. Taboury, *Measuring near field coseismic displacements from SAR images: application to the Landers earthquake*, Geophysical Research Letters, 26 (1999), pp. 3017–3020.

[7] S. B. DeLong, A. Donnellan, D. J. Ponti, R. S. Rubin, J. J. Lienkaemper, C. S. Prentice, T. E. Dawson, G. Seitz, D. P. Schwartz, K. W. Hudnut, et al., *Tearing the terroir: details and implications of surface rupture and deformation from the 24 August 2014 M6.0 South Napa earthquake, California*, Earth and Space Science, 3 (2016), pp. 416–430.

[8] S. Leprince, S. Barbot, F. Ayoub, and J. Avouac, *Automatic and precise orthorectification, coregistration, and subpixel correlation of satellite images, application to ground deformation measurements*, IEEE Transactions on Geoscience and Remote Sensing, 45 (2007), pp. 1529–1558.

[9] N. Ekhtari and C. Glennie, *High-resolution mapping of near-field deformation with airborne Earth observation data, a comparison study*, IEEE Transactions on Geoscience and Remote Sensing, 56 (2017), pp. 1598–1614.

[10] W. D. Barnhart, J. R. Murray, S.-H. Yun, J. L. Svarc, S. Samsonov, E. Fielding, B. A. Brooks, and P. Milillo, *Geodetic constraints on the 2014 M6.0 South Napa earthquake*, Seismological Research Letters, 86 (2015), pp. 335–343.

[11] C. W. Milliner, J. F. Dolan, J. Hollingsworth, S. Leprince, F. Ayoub, and C. G. Sammis, *Quantifying near-field and off-fault deformation patterns of the 1992 M_w 7.3 Landers earthquake*, Geochemistry, Geophysics, Geosystems, 16 (2015), pp. 1577–1598.

[12] W. D. Barnhart, R. D. Gold, H. N. Shea, K. E. Peterson, R. W. Briggs, and D. J. Harbor, *Vertical coseismic offsets derived from high-resolution stereogrammetric DSM differencing: The 2013 Baluchistan, Pakistan earthquake*, Journal of Geophysical Research: Solid Earth, 124 (2019), pp. 6039–6055.

[13] C. P. Scott, J. R. Arrowsmith, E. Nissen, L. Lajoie, T. Maruyama, and T. Chiba, *The M7 2016 Kumamoto, Japan, earthquake: 3-D deformation along the fault and within the damage zone constrained from differential lidar topography*, Journal of Geophysical Research: Solid Earth, 123 (2018), pp. 6138–6155.

[14] X. Zhang, C. Glennie, and A. Kusari, *Change detection from differential airborne lidar using a weighted anisotropic iterative closest point algorithm*, IEEE Journal of Selected Topics in Applied Earth Observations and Remote Sensing, 8 (2015), pp. 3338–3346.

[15] C. P. Scott, S. B. DeLong, and J. R. Arrowsmith, *Distribution of aseismic deformation along the Central San Andreas and Calaveras faults from differencing repeat airborne lidar*, Geophysical Research Letters, 47 (2020), e2020GL090628.

[16] E. Nissen, A. K. Krishnan, J. R. Arrowsmith, and S. Saripalli, *Three-dimensional surface displacements and rotations from differencing pre-and post-earthquake lidar point clouds*, Geophysical Research Letters, 39 (2012).

[17] E. Nissen, T. Maruyama, J. R. Arrowsmith, J. R. Elliott, A. K. Krishnan, M. E. Oskin, and S. Saripalli, *Coseismic fault zone deformation revealed with differential lidar: examples from Japanese M_w 7 intraplate earthquakes*, Earth and Planetary Science Letters, 405 (2014), pp. 244–256.

[18] A. K. Krishnan, E. Nissen, S. Saripalli, R. Arrowsmith, and A. H. Corona, *Change detection using airborne lidar: applications to earthquakes*, in Experimental Robotics, Springer, 2013, pp. 733–743.

[19] A. Diederichs, E. Nissen, L. Lajoie, R. Langridge, S. Malireddi, K. Clark, I. Hamling, and A. Tagliasacchi, *Unusual kinematics of the Papatea fault (2016 Kaikōura earthquake) suggest anelastic rupture*, Science Advances, 5 (2019), eaax5703.

[20] P. Glira, N. Pfeifer, C. Briese, and C. Ressl, *Rigorous strip adjustment of airborne laserscanning data based on the ICP algorithm*, ISPRS Annals of Photogrammetry, Remote Sensing & Spatial Information Sciences, 2 (2015).

[21] A. Kusari, C. L. Glennie, B. A. Brooks, and T. L. Ericksen, *Precise registration of laser mapping data by planar feature extraction for deformation monitoring*, PhD thesis, University of Houston, 2015.

[22] S. B. DeLong, J. J. Lienkaemper, A. J. Pickering, and N. N. Avdievitch, *Rates and patterns of surface deformation from laser scanning following the South Napa earthquake, California*, Geosphere, 11 (2015), pp. 2015–2030.

[23] B. A. Brooks, S. E. Minson, C. L. Glennie, J. M. Nevitt, T. Dawson, R. Rubin, T. L. Ericksen, D. Lockner, K. Hudnut, V. Langenheim, et al., *Buried shallow fault slip from the South*

Napa earthquake revealed by near-field geodesy, Science Advances, 3 (2017), e1700525.

[24] J. M. Nevitt, B. A. Brooks, R. D. Catchings, M. R. Goldman, T. L. Ericksen, and C. L. Glennie, *Mechanics of near-field deformation during co-and post-seismic shallow fault slip*, Scientific Reports, 10 (2020), pp. 1–13.

[25] C. R. Qi, H. Su, K. Mo, and L. J. Guibas, *Pointnet: deep learning on point sets for 3D classification and segmentation*, in Proceedings of the IEEE Conference on Computer Vision and Pattern Recognition, 2017, pp. 652–660.

[26] M. A. Fischler and R. C. Bolles, *Random sample consensus: a paradigm for model fitting with applications to image analysis and automated cartography*, Communications of the ACM, 24 (1981), pp. 381–395.

[27] J. Bray, J. Cohen-Waeber, T. Dawson, T. Kishida, and N. Sitar, *Geotechnical engineering reconnaissance of the August 24, 2014 M6 South Napa earthquake*, Geotechnical Extreme Events Reconnaissance (GEER) Association Report Number GEER, 37 (2014).

[28] A. E. Morelan, C. C. Trexler, and M. E. Oskin, *Surface-rupture and slip observations on the day of the 24 August 2014 South Napa earthquake*, Seismological Research Letters, 86 (2015), pp. 1119–1127.

[29] G. Roth and M. D. Levine, *Extracting geometric primitives*, CVGIP: Image Understanding, 58 (1993), pp. 1–22.

[30] T. K. Rockwell, S. Lindvall, T. Dawson, R. Langridge, W. Lettis, and Y. Klinger, *Lateral offsets on surveyed cultural features resulting from the 1999 Izmit and Duzce earthquakes, Turkey*, Bulletin of the Seismological Society of America, 92 (2002), pp. 79–94.

[31] R. B. Rusu, Z. C. Marton, N. Blodow, M. Dolha, and M. Beetz, *Towards 3D point cloud based object maps for household environments*, Robotics and Autonomous Systems, 56 (2008), pp. 927–941.

[32] C. R. Qi, L. Yi, H. Su, and L. J. Guibas, *PointNet++: deep hierarchical feature learning on point sets in a metric space*, arXiv preprint arXiv:1706.02413 (2017).

[33] M. Yousefhussien, D. J. Kelbe, E. J. Ientilucci, and C. Salvaggio, *A multi-scale fully convolutional network for semantic labeling of 3D point clouds*, ISPRS Journal of Photogrammetry and Remote Sensing, 143 (2018), pp. 191–204.

[34] T. Shinohara, H. Xiu, and M. Matsuoka, *FWNet: semantic segmentation for full-waveform lidar data using deep learning*, Sensors, 20 (2020), p. 3568.

[35] C. Wen, X. Li, X. Yao, L. Peng, and T. Chi, *Airborne lidar point cloud classification with global-local graph attention convolution neural network*, ISPRS Journal of Photogrammetry and Remote Sensing, 173 (2021), pp. 181–194.

[36] G. H. Golub and C. F. Van Loan, *Matrix computations, vol. 3*, JHU Press, 2012.

[37] T. M. Brocher, A. S. Baltay, J. L. Hardebeck, F. F. Pollitz, J. R. Murray, A. L. Llenos, D. P. Schwartz, J. L. Blair, D. J. Ponti, J. J. Lienkaemper, et al., *The M_w 6.0 24 August 2014 South Napa earthquake*, Seismological Research Letters, 86 (2015), pp. 309–326.

[38] D. J. Ponti, C. M. Rosa, and J. L. Blair, *The M_w 6.0 South Napa earthquake of August 24, 2014 – observations of surface faulting and ground deformation, with recommendations for improving post-earthquake field investigations*, Tech. rep., US Geological Survey, 2019.

[39] F. S. McFarland, J. J. Lienkaemper, and S. J. Caskey, *Data from theodolite measurements of creep rates on San Francisco Bay region faults, California, 1979–2009*, US Geological Survey Reston, VA, 2009.

[40] G. James, D. Witten, T. Hastie, and R. Tibshirani, *An introduction to statistical learning*, vol. 112, Springer, 2013.

[41] M. E. Oskin, J. R. Arrowsmith, A. H. Corona, A. J. Elliott, J. M. Fletcher, E. J. Fielding, P. O. Gold, J. J. G. Garcia, K. W. Hudnut, J. Liu-Zeng, et al., *Near-field deformation from the El Mayor–Cucapah earthquake revealed by differential lidar*, Science, 335 (2012), pp. 702–705.

[42] Y. Fialko, D. Sandwell, M. Simons, and P. Rosen, *Three-dimensional deformation caused by the Bam, Iran, earthquake and the origin of shallow slip deficit*, Nature, 435 (2005), pp. 295–299.

[43] K. E. Budding, J. Boatwright, R. Sharp, and J. Saxton, *Compilation and analysis of displacement measurements obtained on the Superstition Hills fault zone and nearby faults in Imperial Valley, California, following the earthquakes of November 24, 1987*, Tech. rep., US Geological Survey, 1989.

[44] R. V. Sharp and J. L. Saxton, *Three-dimensional records of surface displacement on the Superstition Hills fault zone associated with the earthquakes of 24 November 1987*, Bulletin of the Seismological Society of America, 79 (1989), pp. 376–389.

[45] J. Boatwright, K. E. Budding, and R. V. Sharp, *Inverting measurements of surface slip on the Superstition Hills fault*, Bulletin of the Seismological Society of America, 79 (1989), pp. 411–423.